

ARTICLE OPEN



Screening transition metal-based polar pentagonal monolayers with large piezoelectricity and shift current

Yaguang Guo¹, Jian Zhou², Huanhuan Xie³, Yanyan Chen³ and Qian Wang³✉

Two-dimensional (2D) materials entirely composed of pentagon motifs are of interest for their wide applications. Here, we demonstrate that in-plane polar symmetry can exist in ternary pentagonal monolayers, where the induced electric polarization is not associated with specific conditions, such as ferroelectric phase transition, strain gradient, and layer stacking, but is an intrinsic structural property coming from the orderly arranged polar bonds. Based on the high-throughput screening method and first-principles calculations, we find eight stable 2D polar transition metal compounds with a number of intriguing properties. In particular, their piezoelectric coefficients are three orders of magnitude larger than those of 2D elemental and binary pentagonal structures, and their bulk photovoltaic shift current can reach up to $300 \mu\text{A V}^{-2}$, superior to that of 2D conventional ferroelectric materials such as GeS. Our identified pentagonal monolayers not only expand the family of 2D pyroelectric materials, but also hold potential for energy conversions.

npj Computational Materials (2022)8:40; <https://doi.org/10.1038/s41524-022-00728-4>

INTRODUCTION

Polar materials with electric polarization exhibit emergent effects and functionalities, which have been found to be crucial for many applications such as sensors, nanogenerators, and energy collectors. In recent years, two dimensional (2D) polar materials have received tremendous attention because spontaneous polarization at the nanoscale has been proved to be stable against the depolarization field^{1–4}, and can facilitate a number of properties distinct from their bulk phases⁵. Moreover, many centrosymmetric bulk materials lose their inversion symmetry when thinned down to single layers⁶, providing the potential platform for the formation of low-dimensional polarized states.

Spontaneous polarization is fundamentally determined by the polar symmetry of a crystalline structure. This can be commonly observed in paraelectric-to-ferroelectric phase transition, where ionic displacement reduces the lattice symmetry from centrosymmetric to polar. Monolayer group IV monochalcogenides (SnSe, SnS, GeSe, and GeS) are the prominent examples, in which phase transition from a square unit cell to a rectangular one occurs at a critical temperature (T_C)⁷, hence creating the ferroelectricity⁸. Such symmetry breaking is also associated with the emergence of many interesting properties, including large piezoelectric⁹, pyroelectric¹⁰, and bulk photovoltaic effects (BPVE)¹¹, which are superior to those of 2D non-polar materials^{12,13}. In addition, polar symmetry can also be achieved by external stimulus. It has been found that strain gradient is a promising technique to generate the macroscopic polarization, which is the flexoelectric effect. Unlike piezoelectricity depending on the system lacking inversion center, flexoelectricity can exist in materials of any symmetry. For instance, by bending the nanoribbon of centrosymmetric 2D black phosphorous (BP), the induced strain gradient can lead to electric polarization in the out-of-plane direction¹⁴. Moreover, layer stacking can play a similar role in terms of symmetry engineering. A recent experimental study showed that the in-plane polarization can be formed at the interface of 2D WSe_2/BP

heterojunction, where the emergence of a strong BPVE is observed¹⁵.

Although electric polarization in 2D systems can be realized by the above-mentioned approaches, the existence of polar symmetry requires certain conditions. It is known that spontaneous polarization vanishes in ferroelectric materials when the temperature is above the Curie point; the flexoelectric effect usually relies on a complicated setup for inducing large strain gradients, and the polar interface requires the precise control to achieve the specific stacking pattern of 2D materials. These limitations impede the practical applications for real devices. In this regard, alternatives with intrinsic permanent polar symmetry, the so-called pyroelectric materials, are highly desired. However, much less effort has been made in this field. The only studied 2D material is the Janus MoSSe monolayer^{16,17}, which adopts the sandwiched structure similar to the 2H phase of MoS_2 , but with one S layer replaced by Se atoms. The surface asymmetry gives rise to the formation of vertical permanent dipole moments. Nevertheless, the spatial separation of electrons and holes in the out-of-plane direction is usually suppressed by the extreme thickness of 2D structures, therefore the responses of polarization, such as pyroelectric and piezoelectric coefficients, are rather small in the Janus sheets^{10,18}. On the other hand, since most 2D materials are constructed by the highly symmetric hexagonal motifs¹⁹, the in-plane permanent polar symmetry is rarely seen in 2D materials.

In this work, we show that such polar symmetry can be realized by employing the 2D structures entirely composed of pentagon motifs (referred as pentagonal structure). The basic pattern for generating in-plane permanent polarization is proposed. According to it, we have found a series of ternary 2D transition metal-based pyroelectric materials by using our high-throughput screening method. More importantly, these systems exhibit large piezoelectric and bulk photovoltaic effects, showing great potential for energy conversion applications.

¹Department of Physics, School of Science, Beijing Jiaotong University, Beijing 100044, China. ²Center for Alloy Innovation and Design, State Key Laboratory for Mechanical Behavior of Materials, Xi'an Jiaotong University, Xi'an 710049, China. ³CAPT, School of Materials Science and Engineering, Peking University, Beijing 100871, China.

✉email: qianwang2@pku.edu.cn

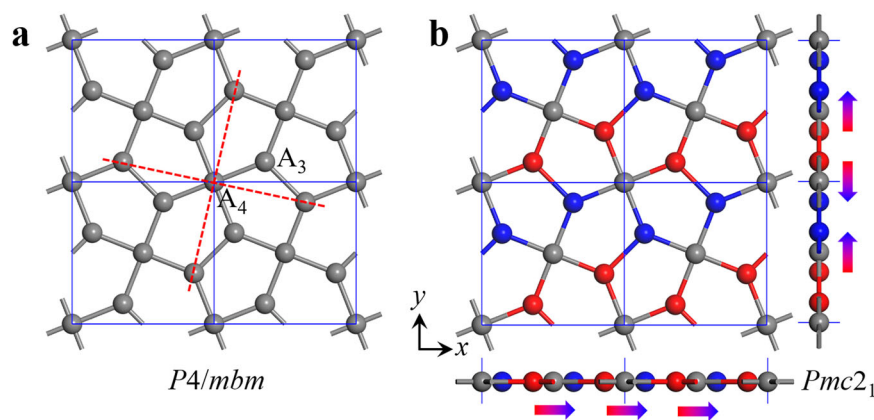


Fig. 1 Basic pattern for inducing in-plane polarization in pentagonal sheet. **a** Monatomic planar pentagonal structure with space group of $P4/mbm$. The red dashed lines show the inversion symmetry about A_4 atoms. **b** Proposed pentagon-based 2D structural model with in-plane polarization. The A_3 sites are occupied with two different elements, and marked in red and blue, respectively.

RESULTS AND DISCUSSION

Basic pattern for inducing in-plane polarization

Since penta-graphene was proposed²⁰, many other 2D pentagonal materials have been theoretically predicted or experimentally synthesized, as summarized in our database²¹. One of the main structural differences among them is the buckling pattern in the out-of-plane direction, while the 2D projections of all these structures resemble the Cairo pentagonal tessellation (see Supplementary Fig. 1). Hence, we use a planar model to discuss the creation of in-plane polarization for simplicity.

We begin with a monatomic planar structure, as shown in Fig. 1a. The six atoms in a unit cell can be divided into two sub-lattices, respectively composed of the three- (A_3) and four-fold coordinated atoms (A_4). The space group is $P4/mbm$ (No. 127) containing an inversion operation, making it a non-polar system. It is known that the appearance of spontaneous polarization in a crystal requires the polar bonds to be properly arranged in a non-centrosymmetric system. In this structural model, the inversion center is located at the A_4 site, so each A_3 atom is inverted to its opposite one (marked by red dashed lines), instead of self-inversion. Therefore, introducing two different elements on the neighboring A_3 sites can simultaneously break the centrosymmetry and form polar bonds. Figure 1b shows the proposed structure, in which the lattice symmetry is reduced to $Pmc2_1$ (No. 26). Due to the perpendicular alignment of A_3 - A_3 bonds, one can see that the electric polarization is cancelled along the y -direction but can be remained in the x -direction. Different from 2D ferroelectric materials, such polarization results from the orderly arranged polar bonds rather than the mechanism of ionic displacement, thus this presented pentagonal structure belongs to the pyroelectric system. Note that due to the similar 2D projection of pentagonal sheets, this pattern can be applied to all 2D pentagonal materials no matter how the buckling is in the out-of-plane direction.

Identification of ternary pentagonal monolayers

Figure 1b gives us a hint that the ternary compounds are the potential candidates for polarized pentagonal sheets, as one can see the three colored atoms. In our previous studies, two ternary pentagonal monolayers (penta-BCN²², and penta-CNP²³) have been predicted by using the atomic substitution and molecule assembling methods. However, it is known that Cairo tessellation commonly exists in the pyrite (FeS_2) and arsenopyrite ($FeAsS$) structures as a hidden layer (see Supplementary Fig. 2), and recent advances have been made in the experimental synthesis of 2D penta-PdSe₂²⁴ and penta-NiN₂¹⁹ sheets, which suggest that

pentagon motifs could be more preferred in transition metal compounds. From this perspective, we try to find stable ternary pentagonal monolayers containing transition metal elements via a high-throughput screening process. Our main idea is that many 2D materials have their parent bulk counterparts, so it is possible to obtain these 2D systems by using physical or chemical exfoliation techniques. Therefore, we aim to search the bulk crystals composed of ternary pentagonal layers.

Figure 2 plots the screening process, in which the searching protocol starts from an initial set of crystals extracted from the Materials Project (MP) Database²⁵. Entries with one transition metal and two different non-metal elements are retrieved, where we only consider the compounds matching the experimentally determined materials in the Inorganic Crystal Structure Database (ICSD)²⁶, and with an energy above convex hull less than 50 meV. Such constraints are able to ensure the thermodynamic stability of the selected materials. Under these conditions, the initial dataset provides a starting point of 307 bulk structures that can be analyzed to find the target candidates.

In an effort to discover ternary compounds with pentagonal layers, the space group ($P2_1/c$, No. 14) was used as the descriptor to search bulk materials with arsenopyrite configuration in the previous study²⁷. However, this method has two limitations that not all materials with $P2_1/c$ symmetry have the arsenopyrite structure and not all ternary compounds with inside pentagonal layers solely exist in the $P2_1/c$ lattice. In order to make a more comprehensive screening, we designed an approach to identify the target structures. The first step is to extract a single layer from the bulk materials. As illustrated in Fig. 2, when the cutting plane is parallel to the (001) surface, the atomic coordinates within the unit cell will be rearranged in descending order of the components along the [001] direction (see Supplementary Fig. 3). Because there are six atoms in a unit cell of the pentagonal sheet, we pick out the first six atoms and project them onto 2D plane. Then we compare the symmetry between the projected structure and the proposed one (Fig. 1b). If the projected monolayer has the $Pmc2_1$ symmetry, its corresponding bulk phase will be regarded as the target candidate. Note that this step of symmetry comparison can ensure the A_3 - A_3 bonds being polarized, excluding the possibility that the neighboring A_3 atoms are with same elements (see Supplementary Fig. 4). Since the cleavage can be along any direction, we also consider the cutting plane parallel to the (100) and (010) surfaces, and use the similar procedure to identify the target bulk materials.

By applying the full protocol to all 307 bulk structures in the initial dataset, we identify 66 materials that have the pentagonal tessellations as shown in Supplementary Table 1. In terms of their

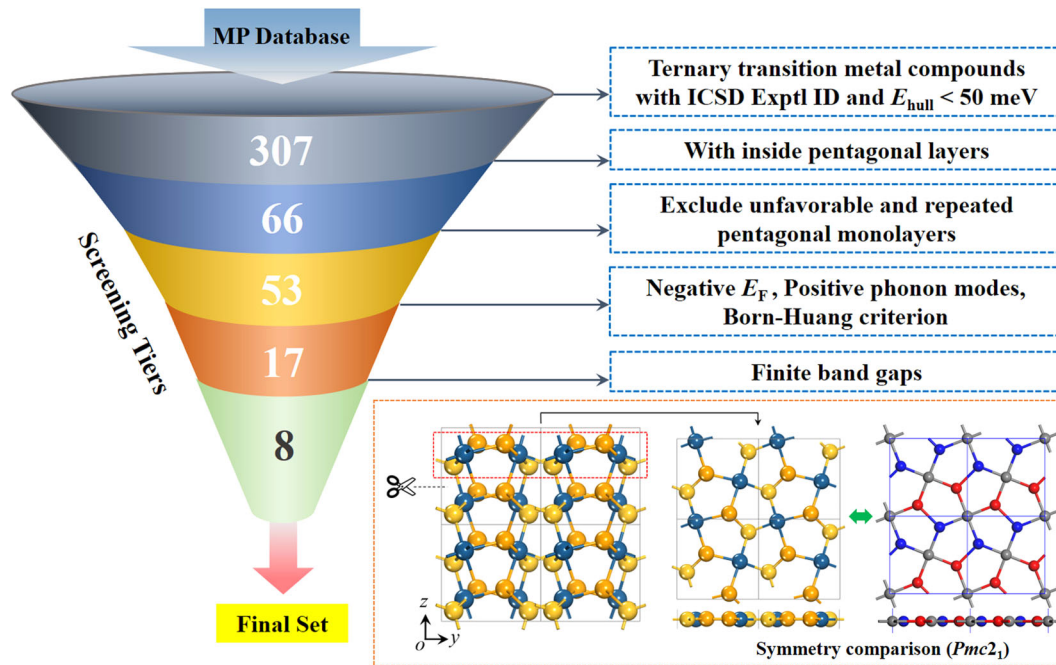


Fig. 2 High-throughput screening funnel for the ternary pentagonal semiconducting monolayers. The scheme of searching for such sheet from a bulk compound composed of pentagonal layers is presented in the orange dashed box.

lattice symmetries, these materials are classified into seven sets with space groups of $P2_1/c$, $P2_12_12_1$, $Pca2_1$, $Pmn2_1$, $Pbcn$, $Pbca$, and $P2_13$ (see Supplementary Fig. 5). The description of these systems can be seen in the Supplementary Information. One can see that our results not only reproduce the arsenopyrite-like materials with $P2_1/c$ symmetry reported by the previous work²⁷, but also find another six types of bulk crystals with inside pentagonal layers, hence indicating the reliability and feasibility of our approach. Generally, the screened systems are composed of group VIII B, group V, and group VI elements with a non-layered structure, while some exceptions occur in Pt-IV-VI compounds. In addition, a layered crystal of PdSse is identified, which can be seen as a derivative of PdSe₂²⁴.

In the next step, the pentagonal monolayers are obtained by exfoliating the 66 identified bulk materials. After fully geometry optimization, we obtain 53 distinct 2D ternary structures by excluding the unfavorable and repeated configurations. To evaluate the thermodynamic stability, we calculate their formation energies (E_F) by using the following definition:

$$E_F = \{E_{\text{tot}} - 2 \times (E_M + E_A + E_B)\} / 6, \quad (1)$$

where E_{tot} is the total energy of the ternary system, E_M , E_A , and E_B are the energy per atom of the transition metal and two non-metal elements in their ground state bulk phases, respectively. As shown in Fig. 3, negative E_F is found in most Nickel-group (Ni, Pd, and Pt) compounds and a small part of Cobalt- and Iron-group (Co, Rh, and Fe) compounds, which are considered as the energetically favorable candidates. To check their dynamic and mechanical stabilities, we then calculate the phonon spectra and elastic coefficients for the screened systems. Results are summarized in Supplementary Fig. 6 and Supplementary Table 2. Materials, without imaginary vibrational frequencies and satisfying the Born-Huang criterion²⁸ ($C_{11}C_{22} - C_{12}^2 > 0$ and $C_{66} > 0$), are considered to be both dynamically and mechanically stable. These combined criteria reduce the original set of the 53 monolayers to the 17 stable structures, as marked by the blue bars in Fig. 3.

Besides the non-centrosymmetry, another condition for electric polarization is that a material should be nonconductive. By employing both the PBE and HSE06 functionals, finite band gaps

are found for eight structures, i.e., penta-CoPSe, CoAsS, RhSbS, RhPSe, PdSse, PtGeS, PtSiSe, and PtSiTe (red marked in the caption of Fig. 3), which therefore can be regarded as 2D pyroelectric materials possessing permanent polarization. The band gaps calculated at the HSE06 level are in the range from 0.79 to 2.17 eV (see Supplementary Table 2), well matching the infrared and visible light window, hence could be beneficial for optoelectronics. Because pyroelectric polarization is an intrinsic structural property, the thermal stabilities of the screened systems are further examined by performing the ab initio molecular dynamics (AIMD) simulations using the canonical (NVT) ensemble²⁹. The results (see Supplementary Figs. S7 and S8) show that except penta-CoPSe, all the other seven semiconducting pentagonal structures can withstand temperatures at least up to 1500 K, which is larger than the Curie temperatures of many 2D ferroelectric materials, such as In₂Se₃³⁰, elemental group V monolayers³¹, group IV monochalcogenides³², and group IV tellurides³³, therefore exhibiting great potentials for high-temperature device applications.

Next, we make a few remarks on the preparation of these selected systems. Among them, the most promising one could be the PdSse monolayer as its bulk phase has a vdW layered structure. Previously, Hulliger has demonstrated that the structural configuration of ternary PdSse remains in its two corresponding binary phases^{34,35}, therefore it is expected that the PdSse monolayer can be synthesized by using mechanical exfoliation similar to the case of PdSe₂. The calculated exfoliation energy is 28.01 meV Å⁻², which is close to that of PdSe₂ (26.55 meV Å⁻²) and h-BN (~28 meV Å⁻²)³⁶, indicating the feasibility of its exfoliation process. For other pentagonal systems, the neighboring layers are covalently bonded in the non-layered bulk structures, thus the corresponding monolayers might be synthesized via a high-pressure technique¹⁹, or chemical method like chemical vapor deposition. We note that some 2D pentagonal transition metal compounds have been proved to be energetically favorable among their allotropes³⁷. So, we further performed a global structure search for the 2D ternary pentagonal compounds using the CALYPSO code. It is found that penta-PtGeS is the ground

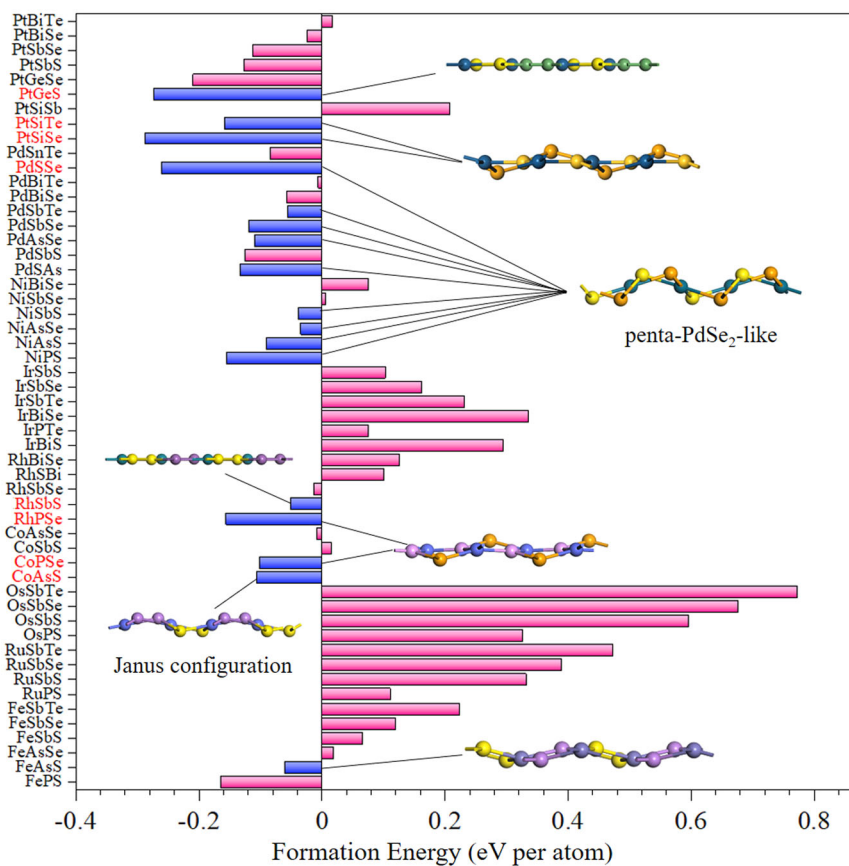


Fig. 3 Formation energy of the 53 ternary 2D pentagonal structures. The blue bars represent the 17 structures that are confirmed to be dynamically and mechanically stable. The compounds marked in red in the caption are semiconductors. The inset images are the side views for the stable structures.

state structure (see Supplementary Fig. 9), thus indicating the feasibility of experimental synthesis of this 2D material, while other structures are in their metastable states.

Geometric structures and mechanical properties

In Fig. 3, we show the side views of the 17 stable monolayers (including the metallic systems). Among them, all Ni- and Pd-based compounds, as well as CoAsS, adopt the penta-PdSe₂-like structure (see Supplementary Fig. 1), namely, the monolayer features a planar tetra-coordination of the transition metal atoms, and puckered pentagons with a vertical buckling. The only difference is that penta-CoAsS has a Janus configuration, i.e., the As and S atoms are respectively located at the top and bottom layers inducing a vertical polarization, while the two surfaces in other systems are equivalent. For 2D ferroelectric materials, switchable dipole moments in both in-plane and out-of-plane directions are found for α -In₂Se₃³⁸. Here, we show that permanent dipole moments along two directions can be realized in pyroelectric penta-CoAsS monolayer. The buckled configuration also exists in penta-FeAsS, CoPSe, RhPSe, PtSiSe, and PtSiTe, and the buckling patterns in these structures are very different from the previously reported 2D pentagonal materials, implying the structural diversity of the pentagonal sheets. In addition, we notice that penta-RhSbS and PtGeS are completely planar, sharing similarity in configuration with the recently synthesized penta-NiN₂ sheet¹⁹ in Cairo tessellation.

The buckled configuration has two effects on the mechanical properties as compared with the planar one. Firstly, the elastic coefficients are generally smaller in buckled structures. A rational understanding is the atomic positions can relax along the vertical

direction, hence structure deformation is prone to happen under external strain. This is beneficial for piezoelectric response, which will be discussed below. Secondly, negative Poisson's ratio (NPR) can be observed in buckled pentagonal sheet²⁰. The elastic coefficient C_{12} is calculated to be negative for penta-PtSiSe, PdSbSe, and PdSbTe (see Supplementary Table 2), which in turn leads to the emergence of NPR along principal axes with values of -0.16 , -0.70 , and -0.38 , respectively. Compare to other 2D materials, such as phosphorene (-0.027)³⁹, silica (-0.123)⁴⁰, and borophane (-0.053)⁴¹, these results imply that the three pentagonal sheets are good 2D auxetic materials with multiple applications in fastener, sensors, and tension activatable substrate.

Electronic properties

To provide insights into the electronic structures of the semiconducting systems, we show the band structures with and without spin-orbit coupling (SOC) of penta-PdSSe as an example in Fig. 4a, and those of the other monolayers in Supplementary Fig. 10. One can see that the SOC effect can lead to a splitting in both the valence and conduction bands ranging from ~ 10 meV (PtGeS) to ~ 230 meV (PtSiSe), which is comparable to the value of transition metal dichalcogenides⁴². This could be appealing for valleytronics due to the broken inversion symmetry in these pentagonal systems. Moreover, the ternary pentagonal structures belong to $P2_1$ or $Pmc2_1$ space group containing screw axis. According to a previous study^{43,44}, such non-symmorphic symmetry operator $\{g|\mathbf{t}\}$ can protect the degeneracies in the invariant lines of the Brillouin zone, where $g\mathbf{k} = \mathbf{k}$. This is the case for the X \rightarrow M path, along which the stick-together bands are observed. The degeneracy is related to a large density of state

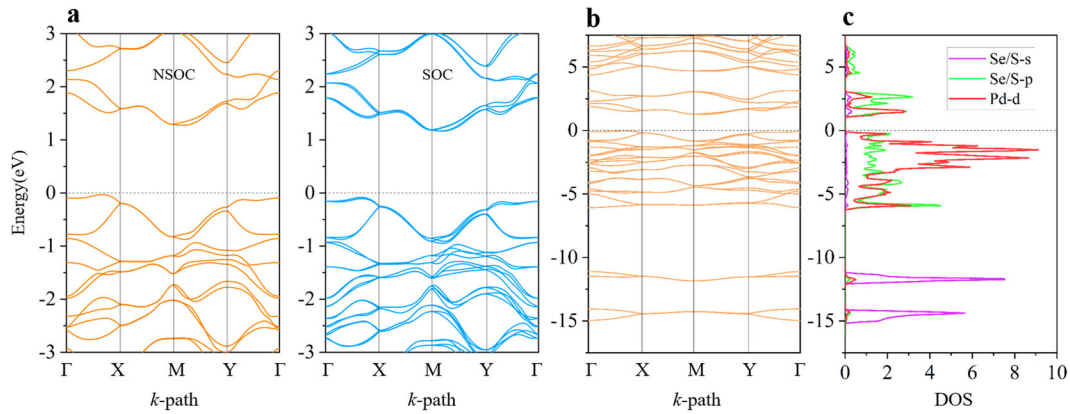


Fig. 4 Electronic properties of penta-PdSSe. a Band structures around the Fermi level with and without SOC. **b** Band structure with all valence bands, and **c** the corresponding partial DOS.

(DOS), thus could lead to enhanced optical responses as will be discussed below. The bonding characters are further explored by considering a wider range of electronic bands. In Fig. 4b, c, it is clear to see that from -15 to -11 eV, the Se/S s orbitals contribute to two sets of deeply localized bands, which respectively correspond to the bonding and antibonding states resulted from the formation of the Se-S bonds. For the range of -6.5 to 3.5 eV, the Pd d orbitals and the Se/S p orbitals play a dominant role. Due to the square-planar coordination of Pd atoms, there are four splitted energy levels (from highest to lowest) for d orbitals: b_{1g} ($d_{x^2-y^2}$), b_{2g} (d_{xy}), a_{1g} (d_{z^2}), and e_g (d_{xz} , d_{yz}). Fatband analysis (see Supplementary Fig. 11) implies that the b_{1g} , b_{2g} , and a_{1g} interact with Se/S p orbitals, forming the lower bonding states (-6.3 to -3.6 eV) and the higher antibonding states (-0.5 to 3 eV), while the e_g contribute to the nonbonding states in the energy window from -3.6 to -0.5 eV. The bandgap is found to lie in the antibonding region, which is also confirmed by the calculated wave functions for the VBM and CBM in Supplementary Fig. 12.

Piezoelectric effect

Piezoelectric response refers to the electric polarization induced by the external strain. All pyroelectric materials can exhibit piezoelectric effects, but are different from ferroelectrics that have a Curie temperature. It has been demonstrated that piezoelectricity can exist in semiconducting 2D materials with pentagraphene-like configuration (see Supplementary Fig. 1), as they belong to the space group of $P-42_1m$ (No. 113) and its subgroups have no inversion center. According to their lattice symmetries, these pentagonal structures have only one effective coefficient e_{36} (d_{36}), implying that the piezoelectric polarization is perpendicular to the sheet. However, the ultrathin configuration of 2D materials usually inhibits the spatial separation of the positive and negative charge centers in the out-of-plane direction⁴⁵, therefore the magnitudes of piezoelectric coefficients are extremely small⁴⁶, e.g., the reported d_{36} for penta-graphene is only 0.065 pm V^{-1} ^{47,48}. For 2D ternary pentagonal sheets, the in-plane inversion symmetry is broken, thus one can expect strong piezoelectric response in these screened materials.

The piezoelectric coefficients are calculated by evaluating the change of polarization in a unit cell under uniaxial strain. For the eight semiconducting pentagonal systems, they all contain C_2 symmetric operation. Here, the in-plane polarization is set to be oriented parallel to the x -axis, thus there are two non-zero piezoelectric tensor components e_{11} and e_{12} . The relationship among elastic (C_{ij}), piezoelectric stress (e_{ij}), and strain coefficients

Table 1. Piezoelectric coefficients for the eight non-metallic ternary pentagonal sheets.

Materials	e_{11} $10^{-10} \text{ C m}^{-1}$	e_{12} $10^{-10} \text{ C m}^{-1}$	C_{11} N m^{-1}	C_{22} N m^{-1}	C_{12} N m^{-1}	d_{11} pm V^{-1}	d_{12} pm V^{-1}
CoPSe	-11.70	-2.03	49.15	100.23	10.14	-23.89	0.38
CoAsS	-8.64	-0.99	66.87	48.84	4.46	-12.87	-0.87
RhSbS	-9.53	1.70	103.72	104.24	37.10	-11.20	5.62
RhPSe	-10.47	1.14	36.71	59.00	7.26	-29.63	5.57
PdSSe	-11.41	-0.46	44.88	68.62	0.64	-25.41	-0.44
PtGeS	-15.03	-0.92	112.47	114.31	41.43	-15.08	4.67
PtSiSe	-19.62	-2.83	32.21	67.78	-5.32	-62.43	-9.08
PtSiTe	-17.07	-1.01	26.99	59.84	3.25	-63.47	1.76

(d_{ij}) can be written as

$$d_{11} = \frac{e_{11}C_{22} - e_{12}C_{12}}{C_{11}C_{22} - C_{12}^2} \text{ and } d_{12} = \frac{e_{12}C_{11} - e_{11}C_{12}}{C_{11}C_{22} - C_{12}^2}. \quad (2)$$

We have listed the values of e_{11} (d_{11}) and e_{12} (d_{12}) in Table 1 and the computational details in Supplementary Fig. 13. As expected, one can see that the piezoelectric coefficients (e_{11} and e_{12}) of the ternary systems are three orders of magnitudes larger than those of the reported elemental and binary penta-graphene-like structures⁴⁷, because there is no spatial limitation for charge redistribution in the basal plane. We find that the value of d_{11} is in the range 11.20 – 63.47 pm V^{-1} , which can reach half of the d_{33} value (130 pm V^{-1}) of lead zirconate titanate (PZT)⁴⁹, and is larger than the values of some prevalent piezoelectric materials, such as α -quartz (2.3 pm V^{-1})⁵⁰, AlN (5.1 pm V^{-1})⁵¹, and ZnO (9.93 pm V^{-1})⁵², hence showing potentials in electromechanical applications. Overall, the eight materials have similar e_{11} coefficients. A slight difference is that the Pt-based structures have larger e_{11} values than the other monolayers. This can be attributed to a larger electronegativity difference between groups IV and VI elements as compared to that of groups V–VI elements (or S–Se). Therefore, it is clear from Eq. 2 that d_{11} is mainly determined by C_{11} , i.e., a smaller C_{11} value leads to a larger d_{11} coefficient. In general, we find that C_{11} has a negative correlation with the sum of the atomic radii except the planar RhSbS and PtGeS (see Supplementary Table 3), thus one can see that the buckled configuration with heavier elements can make the pentagonal structure more flexible, leading to stronger piezoelectric responses. In addition, we notice that the values for e_{11} (d_{11}) are generally larger than those of e_{12} (d_{12}). This is because the

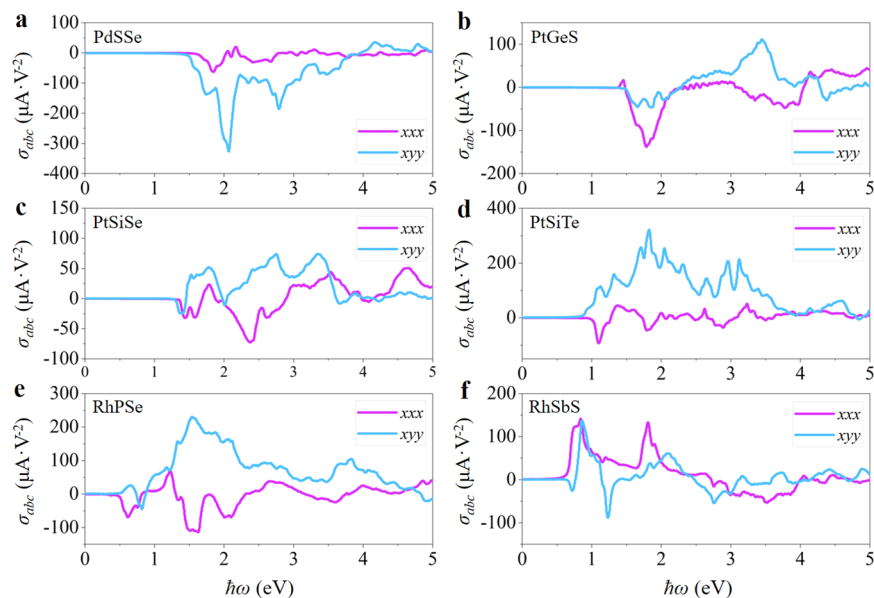


Fig. 5 BPVE response. Components of shift current tensor for pentagonal **a** PdSSe, **b** PtGeS, **c** PtSiSe, **d** PtSiTe, **e** RhPSe, and **f** RhSbS.

polarization origins from the dipole moments on the A_3 – A_3 bonds, the uniaxial strain along polar direction can lead to a larger change of bond length than that along the non-polar direction. In Supplementary Fig. 14, one can see that the Ge–S bond length under 0.5% x -uniaxial strain (polar) is larger than that in y -direction (non-polar), hence a more pronounced change of polarization is found in the former case, leading to a stronger piezoelectric response, i.e., a larger e_{11} (d_{11}) value.

Bulk photovoltaic effect (BPVE)

BPVE is a second order nonlinear optical response that can generate a steady photocurrent in a single-phase material lacking centrosymmetry. Contrary to the p – n junctions, the photo-voltage from BPVE is not constrained by the size of bandgap, therefore such phenomenon is promising for high-efficiency solar cells. Ferroelectrics and piezoelectrics are the mostly studied materials with BPVE. However, the former can only work below the Curie temperature, while the latter cannot respond to the unpolarized sunlight because of the non-polar structure⁵³. In this regard, our screened 2D pentagonal pyroelectric materials are capable to solve both problems. Here, we calculate the shift current tensor σ_{abc} , which has been proved to be one of the major components of BPVE.

The Wannier interpolated band structures with SOC are shown in Supplementary Fig. 10, where the d orbitals for transition metal atoms and p orbitals for non-metal atoms are selected as the projectors according to the fatband analysis (see Supplementary Fig. 11). Note that only non-magnetic pentagonal sheets are considered (see Supplementary Table 2). Figure 5 shows the shift current spectra along the polarization axis under linearly polarized light. For making a quantitative comparison with 3D systems, we rescale the results by assuming an effective thickness with 6 Å, which is estimated by the adjacent layer distance in vdW stacked bulk materials. An overview of σ_{abc} curves suggests that the shift current in ternary pentagonal monolayers can reach up to the order of $10^2 \mu\text{A V}^{-2}$ covering a broad infrared and visible range. Remarkably, significant values are found for the penta-PdSSe, PtSiTe, and RhPSe, in which their xyy components are $326 \mu\text{A V}^{-2}$ at $\hbar\omega = 2.07 \text{ eV}$, $320 \mu\text{A V}^{-2}$ at $\hbar\omega = 1.83 \text{ eV}$, and $231 \mu\text{A V}^{-2}$ at $\hbar\omega = 1.55 \text{ eV}$, respectively. It is known that the low efficiency of photoelectric conversion is the major issue for the BPVE applications. Compare with the most studied ferroelectric

materials, such as perovskite oxides BaTiO_3 ($5 \mu\text{A V}^{-2}$)⁵⁴ and 2D GeS ($\sim 140 \mu\text{A V}^{-2}$)¹¹, the intensities of BPVE exhibited in pentagonal pyroelectric monolayers are relatively large in the same photon energy range. Note that the magnitude of σ_{abc} usually has a negative correlation with the band gap^{55,56}. However, since the PBE functional is used to calculate the shift current in most previous investigations, we believe that the above comparison is acceptable despite the redshift in BPVE response induced by the underestimated gap value.

Next, we explore the microscopic mechanism of the shift current in 2D pentagonal sheets. Similar to the light absorption, the δ -function in Eq. 3 (see “Methods”) indicates that a large joint density of states (JDOS) could be beneficial to improving the shift current, as it represents the resonant band transition. Taking penta-PdSSe as an example. One can see that the main peak-pattern of the shift current is inherited from the JDOS profile as shown in Fig. 6a. The positions of these peaks depend on the van Hove singularities at different band edges. Interestingly, we find that the energy difference ($E_c - E_v$) varies very slowly near the M point (see Fig. 4) because both the valence and conduction bands near the Fermi level show local minima. These bands that tend to track each other give rise to a high JDOS at $\sim 2 \text{ eV}$, which further strongly contribute to the xyy component. In Fig. 6b, we plot the k -resolved shift current at $\hbar\omega = 2.06 \text{ eV}$. It is clear to see that in the momentum space, the major contribution indeed comes from the boundary of the first Brillouin zone, namely, the region around the $M \rightarrow X$ high-symmetry line. Transitions between the four upmost valence bands and four lowest conduction bands play a dominant role, as the total JDOS mainly comes from those energy states (see Fig. 6a). Similar band structures are observed for penta-RhPSe, PtSiSe, and PtSiTe due to the same lattice symmetry. As mentioned earlier, the bands along $M \rightarrow X$ path are stick-together with twofold degeneracy, thus more states can be related by a certain photon energy. From this view, the 2D ternary pentagonal structure might act as a prototype to design potential BPVE materials.

In summary, we have proposed a strategy for introducing in-plane polar symmetry in pentagonal sheets. By using our developed high-throughput screening method, we have identified eight transition metal-based ternary pentagonal monolayers, which can be classified into the category of 2D pyroelectrics due to the formation of permanent polarization. The screened

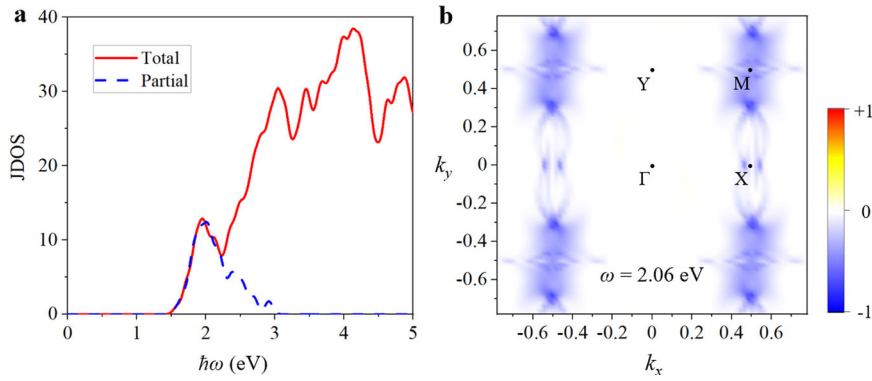


Fig. 6 Analysis of BPVE response. **a** Total JDOS (red solid line) of penta-PdSSe. The blue dashed line shows the contribution from the couplings between upmost four valence bands and lowest four conduction bands. **b** k -resolved shift current for the transition with photon energy of 2.06 eV in penta-PdSSe.

systems are thermally stable and can withstand temperatures up to 1500 K, which is higher than the phase transition temperatures of many 2D ferroelectric materials. By performing first-principles calculations, we demonstrated that these materials have diverse intriguing properties. In particular, penta-PdSSe and PtGeS exhibit good thermodynamic stability, and the buckled penta-PtSiSe, PdSbSe, and PdSbTe possess negative Poisson's ratio. Moreover, the selected semiconducting monolayers possess indirect band gaps ranging from 0.79 to 2.17 eV, which well match the energy window of infrared and visible light, and show stick-together bands at the $X \rightarrow M$ line protected by the non-symmorphic symmetry. Furthermore, due to the in-plane polarization, the identified pentagonal sheets exhibit significant piezoelectric responses (11.20–63.47 pm V^{-1}), which are almost three orders of magnitude larger than those of elemental and binary pentagonal structures. Equally important, these 2D materials also exhibit strong BPVE response with the maximum shift current of 300 $\mu A V^{-2}$ because of the large JDOS from the boundary of the Brillouin zone. Our study demonstrates that 2D pentagonal configurations provide a platform for introducing in-plane permanent polarization, adding some members with good properties to the pyroelectrics family, thus further expanding the applications of 2D pentagonal materials for energy conversions.

METHODS

Electronic properties

First-principles calculations based on density functional theory are carried out by using the Vienna ab initio simulation package (VASP)⁵⁷. Projector augmented wave (PAW) method⁵⁸ is applied to treat interactions between ion and valence electrons. The electronic exchange-correlation interaction is treated by the Perdew–Burke–Ernzerhof (PBE) functional within the generalized gradient approximation (GGA)⁵⁹. The hybrid functional (HSE06)⁶⁰ is also applied to obtain more accurate band structures. The kinetic energy cutoff is set to be 500 eV, and the Monkhorst-Pack k -point mesh⁶¹ with density of $2\pi \times 0.01 \text{ \AA}^{-1}$ is selected to sample the Brillouin zone. For geometry optimization, the convergence threshold for atomic force and energy is 0.01 eV \AA^{-1} and 1×10^{-4} eV, respectively. To reduce the interaction between two adjacent layers, a vacuum space of more than 20 \AA is used in the non-periodic direction. The Berry phase method⁶² implemented in VASP is employed to calculate the intrinsic electric polarization.

Phonon dispersions

The dynamic stability is examined by calculating the phonon spectrum. A large 3×3 supercell is used in the finite displacement method as implemented in the PHONOPY program⁶³.

Global structure search

We employ the particle swarm optimization (PSO) technique implemented in the Crystal structure Analysis by Particle Swarm Optimization (CALYPSO) code^{64–66} to seek for the low-energy structures of the 2D ternary transition metal-based compounds in order to further check whether the pentagonal structure is in its ground state with good energetic stabilities.

Shift current

The shift current conductance σ_{abc} is a third rank tensor^{67,68}. The interband contribution is given by

$$\sigma_{abc}(0; \omega, -\omega) = -\frac{i\pi e^3}{2\hbar^2} \int \frac{dk}{8\pi^3} \sum_{nm} f_{nm} \left(r_{nm}^b r_{nm;a}^c + r_{nm}^c r_{nm;a}^b \right) \delta(\omega_{mn} - \omega), \quad (3)$$

where r_{mn}^a is the element of position matrix. The $r_{mn;b}^a$ is the generalized derivatives with the definition of $r_{mn;b}^a = \frac{\partial r_{mn}^a}{\partial k^b} - i(A_{nn}^b - A_{mm}^b) r_{nm}^a$, where A_{nm}^a is the Berry connection. $f_{nm} = f_n - f_m$ and $\hbar\omega_{mn} = E_m - E_n$ are the differences between occupation factors and band energies. For a more efficient scheme to calculate the shift current conductance, we employed the Wannier-interpolated models proposed by Julen et al.⁶⁹, where the WANNIER90 code⁷⁰ is used to obtain the Wannier functions. The k -grid convergence for integrating Eq. 3 is carefully tested, where we use a $100 \times 100 \times 1$ k -grid to perform the simulation. For 2D system, an effective layer thickness (d) is employed to obtain a bulk-like optical response, where $\sigma_{\text{bulk}}^{abc} = \left(\frac{d_{\text{np}}}{d}\right) \sigma_{2D}^{abc}$ with d_{np} as the lattice length along the non-periodic direction⁷¹.

DATA AVAILABILITY

The datasets generated and/or analyzed during the current study are available from the corresponding author upon reasonable request.

CODE AVAILABILITY

All code used to calculate the current results is available from the corresponding author upon reasonable request.

Received: 21 November 2021; Accepted: 13 February 2022;

Published online: 15 March 2022

REFERENCES

- Fong, D. D. et al. Ferroelectricity in ultrathin perovskite films. *Science* **304**, 1650–1653 (2004).
- Gruverman, A. et al. Tunneling electroresistance effect in ferroelectric tunnel junctions at the nanoscale. *Nano Lett.* **9**, 3539–3543 (2009).
- Hu, W. J., Wang, Z., Yu, W. & Wu, T. Optically controlled electroresistance and electrically controlled photovoltage in ferroelectric tunnel junctions. *Nat. Commun.* **7**, 1–9 (2016).

4. Lee, D. et al. Emergence of room-temperature ferroelectricity at reduced dimensions. *Science* **349**, 1314–1317 (2015).
5. Cui, C., Xue, F., Hu, W.-J. & Li, L.-J. Two-dimensional materials with piezoelectric and ferroelectric functionalities. *NPJ 2D Mater. Appl.* **2**, 1–14 (2018).
6. Hinchet, R., Khan, U., Falconi, C. & Kim, S.-W. Piezoelectric properties in two-dimensional materials: Simulations and experiments. *Mater. Today* **21**, 611–630 (2018).
7. Mehboudi, M. et al. Structural phase transition and material properties of few-layer monochalcogenides. *Phys. Rev. Lett.* **117**, 246802 (2016).
8. Fei, R., Kang, W. & Yang, L. Ferroelectricity and phase transitions in monolayer group-IV monochalcogenides. *Phys. Rev. Lett.* **117**, 097601 (2016).
9. Fei, R., Li, W., Li, J. & Yang, L. Giant piezoelectricity of monolayer group IV monochalcogenides: SnSe, SnS, GeSe, and GeS. *Appl. Phys. Lett.* **107**, 173104 (2015).
10. Liu, J. & Pantelides, S. T. Mechanisms of pyroelectricity in three- and two-dimensional materials. *Phys. Rev. Lett.* **120**, 207602 (2018).
11. Rangel, T. et al. Large bulk photovoltaic effect and spontaneous polarization of single-layer monochalcogenides. *Phys. Rev. Lett.* **119**, 067402 (2017).
12. Duerloo, K.-A. N., Ong, M. T. & Reed, E. J. Intrinsic piezoelectricity in two-dimensional materials. *J. Phys. Chem. Lett.* **3**, 2871–2876 (2012).
13. Schankler, A. M., Gao, L. & Rappe, A. M. Large bulk piezophotovoltaic effect of monolayer 2H-MoS₂. *J. Phys. Chem. Lett.* **12**, 1244–1249 (2021).
14. Pandey, T., Covaci, L., Milošević, M. & Peeters, F. Flexoelectricity and transport properties of phosphorene nanoribbons under mechanical bending. *Phys. Rev. B* **103**, 235406 (2021).
15. Akamatsu, T. et al. A van der Waals interface that creates in-plane polarization and a spontaneous photovoltaic effect. *Science* **372**, 68–72 (2021).
16. Zhang, J. et al. Janus monolayer transition-metal dichalcogenides. *ACS Nano* **11**, 8192–8198 (2017).
17. Lu, A.-Y. et al. Janus monolayers of transition metal dichalcogenides. *Nat. Nanotechnol.* **12**, 744–749 (2017).
18. Dong, L., Lou, J. & Shenoy, V. B. Large in-plane and vertical piezoelectricity in Janus transition metal dichalcogenides. *ACS Nano* **11**, 8242–8248 (2017).
19. Bykov, M. et al. Realization of an ideal Cairo tessellation in nickel diazenide NiN₂: High-pressure route to pentagonal 2D materials. *ACS Nano* **15**, 13539–13546 (2021).
20. Zhang, S. et al. Penta-graphene: A new carbon allotrope. *Proc. Nat. Acad. Sci. USA* **112**, 2372–2377 (2015).
21. Wang, Q. Database for pentagon-based sheets. <http://www.pubsdb.com/>.
22. Zhao, K. et al. Penta-BCN: A new ternary pentagonal monolayer with intrinsic piezoelectricity. *J. Phys. Chem. Lett.* **11**, 3501–3506 (2020).
23. Sun, W., Shen, Y., Guo, Y., Chen, Y. & Wang, Q. 1, 2, 4-Azadiphosphole-based piezoelectric penta-CNP sheet with high spontaneous polarization. *Appl. Sur. Sci.* **554**, 149499 (2021).
24. Oyedele, A. D. et al. PdSe₂: Pentagonal two-dimensional layers with high air stability for electronics. *J. Am. Chem. Soc.* **139**, 14090–14097 (2017).
25. Jain, A. et al. Commentary: The Materials Project: A materials genome approach to accelerating materials innovation. *APL Mater.* **1**, 011002 (2013).
26. Hellenbrandt, M. The inorganic crystal structure database (ICSD)—present and future. *Crystallogr. Rev.* **10**, 17–22 (2004).
27. Liu, L. & Zhuang, H. L. Computational prediction and characterization of two-dimensional pentagonal arsenopyrite FeAsS. *Comp. Mater. Sci.* **166**, 105–110 (2019).
28. Ding, Y. & Wang, Y. Density functional theory study of the silicene-like SiX and XSi₃ (X = B, C, N, Al, P) honeycomb lattices: The various buckled structures and versatile electronic properties. *J. Phys. Chem. C* **117**, 18266–18278 (2013).
29. Nosé, S. A unified formulation of the constant temperature molecular dynamics methods. *J. Chem. Phys.* **81**, 511–519 (1984).
30. Zheng, C. et al. Room temperature in-plane ferroelectricity in van der Waals In₂Se₃. *Sci. Adv.* **4**, eaar7720 (2018).
31. Xiao, C. et al. Elemental ferroelectricity and antiferroelectricity in Group-V monolayer. *Adv. Funct. Mater.* **28**, 1707383 (2018).
32. Mehboudi, M. et al. Two-dimensional disorder in black phosphorus and monochalcogenide monolayers. *Nano Lett.* **16**, 1704–1712 (2016).
33. Wan, W., Liu, C., Xiao, W. & Yao, Y. Promising ferroelectricity in 2D group IV tellurides: A first-principles study. *Appl. Phys. Lett.* **111**, 132904 (2017).
34. Kempf, R., Kuc, A. & Heine, T. Two-dimensional noble-metal chalcogenides and phosphochalcogenides. *Angew. Chem. Int. Ed.* **59**, 9242–9254 (2020).
35. Hulliger, F. Electrical properties of some nickel-group chalcogenides. *J. Phys. Chem. Solids* **26**, 639–645 (1965).
36. Jung, J. H., Park, C.-H. & Ihm, J. A rigorous method of calculating exfoliation energies from first principles. *Nano Lett.* **18**, 2759–2765 (2018).
37. Shen, Y., Guo, Y. & Wang, Q. Large out-of-plane second harmonic generation susceptibility in penta-ZnS₂ sheet. *Adv. Theor. Simul.* **3**, 2000027 (2020).
38. Ding, W. et al. Prediction of intrinsic two-dimensional ferroelectrics in In₂Se₃ and other III₂-VI₃ van der Waals materials. *Nat. Commun.* **8**, 1–8 (2017).
39. Jiang, J.-W. & Park, H. S. Negative Poisson's ratio in single-layer black phosphorus. *Nat. Commun.* **5**, 1–7 (2014).
40. Gao, Z., Dong, X., Li, N. & Ren, J. Novel two-dimensional silicon dioxide with in-plane negative Poisson's ratio. *Nano Lett.* **17**, 772–777 (2017).
41. Kou, L. et al. Auxetic and ferroelastic borophane: A novel 2D material with negative Poisson's ratio and switchable Dirac transport channels. *Nano Lett.* **16**, 7910–7914 (2016).
42. Košmider, K., González, J. W. & Fernández-Rossier, J. Large spin splitting in the conduction band of transition metal dichalcogenide monolayers. *Phys. Rev. B* **88**, 245436 (2013).
43. Young, S. M. & Kane, C. L. Dirac semimetals in two dimensions. *Phys. Rev. Lett.* **115**, 126803 (2015).
44. Zhang, S., Zhou, J., Wang, Q. & Jena, P. Beyond graphitic carbon nitride: Nitrogen-rich penta-CN₂ sheet. *J. Phys. Chem. C* **120**, 3993–3998 (2016).
45. Sanders, N., Bayerl, D., Shi, G., Mengle, K. A. & Kioupakis, E. Electronic and optical properties of two-dimensional GaN from first-principles. *Nano Lett.* **17**, 7345–7349 (2017).
46. Guo, Y., Zhu, H. & Wang, Q. Piezoelectric effects in surface-engineered two-dimensional group III nitrides. *ACS Appl. Mater. Interfaces* **11**, 1033–1039 (2018).
47. Guo, S.-D. & Wang, S.-Q. Tuning pure out-of-plane piezoelectric effect of penta-graphene: A first-principle study. *J. Phys. Chem. Solids* **140**, 109375 (2020).
48. Jia, H.-J. et al. Piezoelectric and polarized enhancement by hydrofluorination of penta-graphene. *Phys. Chem. Chem. Phys.* **20**, 26288–26296 (2018).
49. Fraga, M. A., Furlan, H., Pessoa, R. & Massi, M. Wide bandgap semiconductor thin films for piezoelectric and piezoresistive MEMS sensors applied at high temperatures: an overview. *Microsyst. Technol.* **20**, 9–21 (2014).
50. Bechmann, R. Elastic and piezoelectric constants of alpha-quartz. *Phys. Rev.* **110**, 1060 (1958).
51. Lueng, C., Chan, H. L., Surya, C. & Choy, C. Piezoelectric coefficient of aluminum nitride and gallium nitride. *J. Appl. Phys.* **88**, 5360–5363 (2000).
52. Zhao, M.-H., Wang, Z.-L. & Mao, S. X. Piezoelectric characterization of individual zinc oxide nanobelt probed by piezoresponse force microscope. *Nano Lett.* **4**, 587–590 (2004).
53. Tan, L. Z. et al. Shift current bulk photovoltaic effect in polar materials-hybrid and oxide perovskites and beyond. *NPJ Comp. Mater.* **2**, 1–12 (2016).
54. Young, S. M. & Rappe, A. M. First principles calculation of the shift current photovoltaic effect in ferroelectrics. *Phys. Rev. Lett.* **109**, 116601 (2012).
55. Cook, A. M., Fregoso, B. M., De Juan, F., Coh, S. & Moore, J. E. Design principles for shift current photovoltaics. *Nat. Commun.* **8**, 1–9 (2017).
56. Tan, L. Z. & Rappe, A. M. Upper limit on shift current generation in extended systems. *Phys. Rev. B* **100**, 085102 (2019).
57. Kresse, G. & Furthmüller, J. Efficient iterative schemes for ab initio total-energy calculations using a plane-wave basis set. *Phys. Rev. B* **54**, 11169 (1996).
58. Blöchl, P. E. Projector augmented-wave method. *Phys. Rev. B* **50**, 17953 (1994).
59. Perdew, J. P., Burke, K. & Ernzerhof, M. Generalized gradient approximation made simple. *Phys. Rev. Lett.* **77**, 3865 (1996).
60. Heyd, J., Scuseria, G. E. & Ernzerhof, M. Hybrid functionals based on a screened Coulomb potential. *J. Chem. Phys.* **118**, 8207–8215 (2003).
61. Monkhorst, H. J. & Pack, J. D. Special points for Brillouin-zone integrations. *Phys. Rev. B* **13**, 5188 (1976).
62. King-Smith, R. & Vanderbilt, D. Theory of polarization of crystalline solids. *Phys. Rev. B* **47**, 1651 (1993).
63. Togo, A., Oba, F. & Tanaka, I. First-principles calculations of the ferroelastic transition between rutile-type and CaCl₂-type SiO₂ at high pressures. *Phys. Rev. B* **78**, 134106 (2008).
64. Wang, Y., Lv, J., Zhu, L. & Ma, Y. Crystal structure prediction via particle-swarm optimization. *Phys. Rev. B* **82**, 094116 (2010).
65. Wang, Y., Lv, J., Zhu, L. & Ma, Y. CALYPSO: A method for crystal structure prediction. *Comput. Phys. Commun.* **183**, 2063–2070 (2012).
66. Lv, J., Wang, Y., Zhu, L. & Ma, Y. Particle-swarm structure prediction on clusters. *J. Chem. Phys.* **137**, 084104 (2012).
67. Sipe, J. & Shkrebti, A. Second-order optical response in semiconductors. *Phys. Rev. B* **61**, 5337 (2000).
68. Pan, Y. & Zhou, J. Toggling valley-spin locking and nonlinear optical properties of single-element multiferroic monolayers via light. *Phys. Rev. Appl.* **14**, 014024 (2020).
69. Ibañez-Azpiroz, J., Tsirkin, S. S. & Souza, I. Ab initio calculation of the shift photocurrent by Wannier interpolation. *Phys. Rev. B* **97**, 245143 (2018).
70. Mostofi, A. A. et al. An updated version of wannier90: A tool for obtaining maximally-localised Wannier functions. *Comput. Phys. Commun.* **185**, 2309–2310 (2014).
71. Mu, X., Pan, Y. & Zhou, J. Pure bulk orbital and spin photocurrent in two-dimensional ferroelectric materials. *NPJ Comput. Mater.* **7**, 1–10 (2021).

ACKNOWLEDGEMENTS

This work is partially supported by the National Natural Science Foundation of China (Grant Nos. 12104037, 11974270, and 11974028), and the Fundamental Research Funds for the Central Universities (2021JBM041), and it is also supported by the High-Performance Computing Platform of Peking University, China.

AUTHOR CONTRIBUTIONS

Q.W. conceived the concept. Y.G. performed calculations. J.Z. wrote the code for shift current conductance calculation. Y.G., J.Z., H.X., Y.C., and Q.W. analyzed data. Y.G. and Q.W. wrote the manuscript.

COMPETING INTERESTS

The authors declare no competing interests.

ADDITIONAL INFORMATION

Supplementary information The online version contains supplementary material available at <https://doi.org/10.1038/s41524-022-00728-4>.

Correspondence and requests for materials should be addressed to Qian Wang.

Reprints and permission information is available at <http://www.nature.com/reprints>

Publisher's note Springer Nature remains neutral with regard to jurisdictional claims in published maps and institutional affiliations.



Open Access This article is licensed under a Creative Commons Attribution 4.0 International License, which permits use, sharing, adaptation, distribution and reproduction in any medium or format, as long as you give appropriate credit to the original author(s) and the source, provide a link to the Creative Commons license, and indicate if changes were made. The images or other third party material in this article are included in the article's Creative Commons license, unless indicated otherwise in a credit line to the material. If material is not included in the article's Creative Commons license and your intended use is not permitted by statutory regulation or exceeds the permitted use, you will need to obtain permission directly from the copyright holder. To view a copy of this license, visit <http://creativecommons.org/licenses/by/4.0/>.

© The Author(s) 2022